Laminar Flow and Mass Transport in a Twice–Folded Microchannel

Dominik P. J. Barz and Hamid Farangis Zadeh
Forschungszentrum Karlsruhe, Institute for Nuclear and Energy Technologies, P.O.Box 3640, D-76021 Karlsruhe, Germany

Peter Ehrhard
University of Dortmund, Biochemical and Chemical Engineering, Fluid Mechanics, Emil–Figge–Str. 68, D-44221 Dortmund, Germany

DOI 10.1002/aic.11382
Published online December 26, 2007 in Wiley InterScience (www.interscience.wiley.com).

The flow and mass transport within a twice–folded microchannel is investigated. For the measurement of the concentration field the microlaser–induced fluorescence technique (μLIF) is engaged. Microparticle image velocimetry (μPIV) is further employed to obtain the velocity field. Deviation from standard μPIV by seeding a partial stream of the flow only, results in partial velocity profiles. This procedure allows for the observation of the contact interface between the seeded and the unseeded liquid. Distorted contact interfaces is recognized within and after each bend, indicating strong secondary flows. The measurements are compared to numerical simulations, solving for both the flow, and the mass-transport equations, and, subsequently, performing particle tracking. The results are, on one hand, in reasonable agreement with the experiments. On the other hand, the differences between the contact interface from the mass-transport equation and from particle tracking clarifies the effect of diffusion. © 2007 American Institute of Chemical Engineers *AIChE J,* 54: 381–393, 2008
Keywords: microfluidic, folded microchannel, secondary flow, particle image velocimetry, laser–induced fluorescence technique, numerical simulation, particle tracking

Introduction

The relevance of microfluidics is reflected by the growing number of research and development projects in this subject area, and the resulting multitude of technical applications. The advantages of miniaturization are used in the field of microheat exchangers, where the micro channel's high-surface to volume ratio enables a substantial increase of heat transfer.[1] The excellent thermal–management features, further, allow for a safe and efficient process control within microreactors,[2] whose establishment in the chemical industry has just begun. Moreover, in the field of chemical and biological analysis, the use of microfluidic devices proves to be beneficial. This leads to the concept of "micro total analysis systems" (μTAS),[3] which can be also extended to lab processes other than analysis and is called "lab on a chip" (LOC). The application of these concepts does not only allow more operation steps per unit time, it additionally ensures the consumption of fewer reagents and the production of less waste, while at the same time energy consumption is reduced.[4] To fulfil these ambitious demands, several integrated microcomponents, such as pumps, valves, or detectors are arranged on a plastic or glass chip and connected by a system of microchannels. Transport, separation, and focussing of species are typical microfluidic processes that may take place within these chips. Additionally, the

Correspondence concerning this article should be addressed to D. Barz at db455@cornell.edu.
Present address of Dominik P. J. Barz: School of Chemical and Biomolecular Engineering, Cornell University, Ithaca, New York 14853; Electronic address: db455@cornell.edu

rapid mixing of small quantities, in order to reduce analysis and reaction time, is one of the key steps with regard to LOC and μTAS.[5] A typical scenario occurring in microfluidic systems is the mixing of liquids in a flow regime of Reynolds numbers $Re \sim 0.1 - 10$. The transition from laminar to turbulent flow in a (macroscopic) channel arises typically at Reynolds numbers of $Re \sim 10^3 - 10^4$. Hence, in microfluidic systems we are far away from the turbulent flow regime, and no turbulent fluctuations serve to significantly improve mixing. Mixing in microchannels instead proceeds by molecular diffusion across an interfacial area on a relatively long time scale. Thus, one possibility to enhance mass transport is the increase of this interfacial area.

Meisel and Ehrhard[6] have suggested the concept of an electrically–excited micromixer with the objective of application in microfluidic systems. In detail, the mixer comprises a Y–junction and a single meander, i.e., a simple twice–folded channel segment, downstream in the common channel. The mean transport is realized by a pressure–driven base flow. Mixing is improved by applying a time–dependent electrical field, resulting in a superimposed oscillatory electroosmotic flow. The two–dimensional (2-D) simulations of Meisel and Ehrhard indicate clearly that, given a reasonable ratio of pressure–driven base velocity and electroosmotic velocity, the oscillatory electroosmotic flow through the folded channel leads to substantially higher degrees of mixing at the micromixer outlet. Even though 2-D simulations are able to capture the principal mode of operation, a detailed reproduction of the complex 3-D flow field is necessary to compare against experiments: All theoretical research on flows in microchannels needs validation with respect to the assumptions and simplifications, usually used for modeling. Therefore, we shall perform 3-D simulations and compare the results with the corresponding experiment. In this article, we focus on the pure pressure–driven base flow.

Even for the pure pressure–driven base flow, a complex three–dimensional flow field can be expected. Since the work of Dean[7,8] it is well known that curved channels with circular cross sections may result in secondary flows. Dean solved the Navier–Stokes equations analytically for the laminar flow within curved channels of large radii. He found that secondary flows are characterized by the dimensionless parameter $De = Re\sqrt{d_0/r_0}$, these days termed Dean number, where Re is the Reynolds number, d_0 the diameter of the channel, and r_0 the radius of curvature. The analytical solution features two counter–rotating vortices, orthogonally superimposed onto the main flow. This can be explained as follows: (1) The fluid near the center of a curved channel experiences the greatest centrifugal forces due to its greatest axial velocity. This is responsible for the outward movement of this fluid. (2) The replacement fluid meanwhile flows inward along the walls, where the axial velocity, and, hence, centrifugal forces, are smaller. This recirculation flow establishes two counter–rotating vortices, also referred to as Dean vortices. The numerical computations of Joseph et al.[9] showed that Dean vortices arise likewise in curved channels with square cross-sections. Moreover, a secondary flow regime with two pairs of counter–rotating vortices is observed for square cross sections in the range $100 \lesssim De \lesssim 520$. This is also confirmed by the numerical work of Cheng et al.[10] and Ghia and Sokhey.[11] The experimental confirmation of this additional pair of vortices is attained within the Laser–Doppler–anemometry (LDA) experiments of Hille et al.[12] These authors claimed that differences in literature with regard to the Dean number range of the second vortex pair may be attributed to different curvature ratios d_0/r_0. Results may be only comparable if both parameters, Dean number and curvature ratio, are kept identical. Recent numerical work on secondary flows in microchannel of similar geometry is presented by Schoenfeld and Hardt.[13] These authors propose a (chaotic) micromixer, relying on the periodic switching between the secondary flow pattern with one and two pairs of vortices. The laminar flow and the concentration field in a microchannel with hair–pin curves is investigated numerically by Yamaguchi et al.[14] The comparison of the simulated concentration field with experimental results, measured by confocal fluorescence microscopy, shows qualitative agreement. Finally, secondary flows in microchannels are not only advantageous with respect to mixing. They are also beneficial for the designs of chemical reactions at the interface of reactants,[15] or for the extraction between aqueous and organic phases.[16]

A multitude of theoretical and experimental articles on secondary flows in macro channels, and a few on microchannels, are published in literature. Nevertheless, they all relate to smoothly–curved channels, and, to our knowledge, there are no investigations on the flows in sharply–folded microchannels. Further, a quantitative comparison of numerical and experimental results within one article is rather hard to find. This article is organized as follows: (1) The micromixer geometry is introduced. (2) The experimental setup and the simulation methodology are explained. (3) The results of the flow and concentration fields are presented and discussed. (4) A summary and an outlook is given.

Micromixer

The object under investigation is a twice–folded microchannel, the essential fluidic part of the micromixer. The microfluidic chip has been mainly manufactured from *FOTURAN* glass by *mgt mikroglas technik*, Mainz (Germany), and is shown in Figure 1. *FOTURAN* is a photosensitive glass, reacting to UV light (wavelength $\lambda \approx 310\ nm$), and allows for selective etching.[17] The microfluidic chip consists of three glass layers, the micromixer layer, a base, and a cover layer. To realize the micromixer layer, a *FOTURAN* glass layer of thickness $110\ \mu m$ is exposed to UV light through a quartz/chromium mask during a lithographic process. The mask comprises the plane geometry of the micromixer. In detail, the geometry includes two inlet channels forming a Y-junction under an angle of 40°, followed by a common outlet channel. The twice–folded channel segment is located in the outlet channel, at a distance of $130\ \mu m$ downstream to the junction. The channel width is $d_0 = 110\ \mu m$, which in combination with the thickness of the micromixer layer will result in a square microchannel of $110 \times 110\ \mu m^2$ cross section. Following the exposure, the micromixer layer is heated up to $870\ K$, so that the exposed parts of the chip crystallize, while the nonexposed parts retain their glass structure. The crystallized parts are finally etched away in a solution of hydrofluoric acid (HF(aq)), and, thus, the geometric structure of the mask is assigned to the micromixer layer. The base layer is also made from

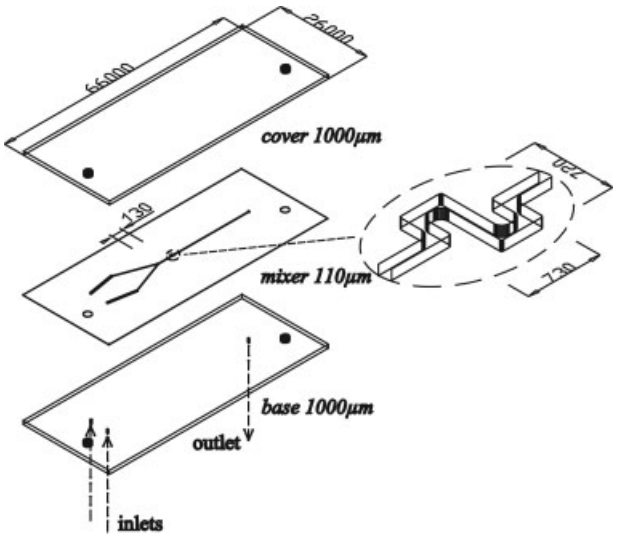

Figure 1. Layers of the microfluidic chip and close–up sketch of the twice–folded channel segment.

FOTURAN; the cover layer, however, is made from *B*270 glass for optical reasons. Both layers have a thickness of 1,000 μm. Several holes are drilled in these layers to enable inflow, outflow, and positioning, respectively. Finally, to seal the etched microchannel structure, the base and the cover layer are attached to the micromixer layer by means of diffusion–bonding.

Experimental Setup

We aim to investigate the concentration field and the flow field within the twice–folded channel segment of the micromixer. The concentration field is measured by means of a micro laser–induced fluorescence method (μLIF), while microparticle image velocimetry (μPIV) is used for the measurement of the velocity field. Hence, an experimental setup, allowing for two measuring techniques on the basis of easy adaption, is used. Figure 2 shows the common experimental setup used for velocity and concentration field measurements. The microfluidic device is mounted onto a PMMA support, containing channels for delivering and discharging the liquid. Syringe pumps (*kd Scientific*), available with different volumes, enable the flow of two liquids through the micromixer. The range of flow rates is $\dot{V} = 0.05 - 20$ ml/h, which corresponds to a range of Reynolds numbers of $Re \simeq 0.1 - 50$. We determine the accuracy to $\Delta\dot{V} = 0.05$ $\mu l/h$ at the lowest flow rate and to $\Delta\dot{V} = 20$ $\mu l/h$ at the highest flow rate. The mass $m(t)$ leaving the microfluidic device is collected and measured by means of a precision scale (*Sartorius*). This balance has an accuracy of $\delta m = 0.01$ mg, and communicates via a RS232 serial interface with LabVIEW (*National Instruments*), the applied data processing software. The mass flow rate is determined from the collected mass Δm per collecting time Δt, according to $\dot{m} = \Delta m/\Delta t$. It should be mentioned that, for proper determination, the flow rate has to be corrected by the evaporation rate. For optical access, an inverted microscope (*Leica, DMIRM*) is used and connected to a CCD camera (*PCO, Image Intense*). The images from the CCD camera are transferred to a computer and analyzed by an image–processing software (*LaVision, DaVis 6.0*). The further setup, i.e., the light source and several optical devices, depends on the object of investigation.

Concentration field

For mass-transport investigations in microfluidic devices, it is important to capture the concentration fields within the microchannels. For this purpose, a concentration field measurement technique (μLIF) has been developed by Matsumoto et al.[18] Provided that an adequate fluorescent dye is chosen, the emitted fluorescence intensity from a mixture of liquid and a fluorescent dye depends on the concentration of the dye, on the pH value, and on the temperature.

Within one of the syringe pumps pure, filtered, and deionized water as non–fluorescent liquid is used. Within the other pump water with the dissolved fluorescent dye *Rhodamine B* is used. *Rhodamine B* can be excited by green light and emits red light with the maximum intensity in the range $\lambda = 575–585$ nm.[19] Therefore, a continuous–wave argon ion laser (*Model 2550, Spectra-Physics*), providing green excitation light at a wavelength of $\lambda = 514$ nm, serves as light source. The green laser beam is expanded through a set of lenses before it is coupled into the microscope and guided coaxially through the objective to the microchannel. We apply a 5× microscope objective, which offers a large field of view. The red fluorescent light from inside of the microchannel is passed back through the microscope and recorded by the CCD camera. A set of optical filters ensures purely–fluorescent (red) light to arrive at the CCD camera and avoids the entry of foreign light into the illumination path. This fluorescence technique collects the emitted fluorescent light from all depths of the microchannel, and, thus, is linked to the height–averaged concentration field. Further, with regard to quantitative results extensive calibration has to be performed. All details of this micro laser–induced fluorescence method can be found in Matsumoto et al.[18]

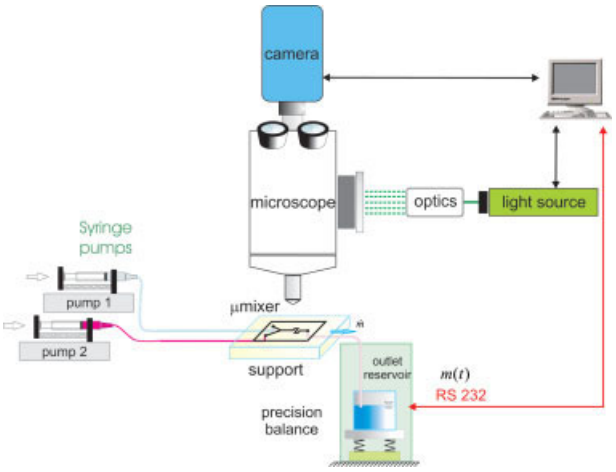

Figure 2. Common experimental setup.

[Color figure can be viewed in the online issue, which is available at www.interscience.wiley.com.]

Velocity field

The velocity field within the twice–folded channel segment is measured by means of microparticle image velocimetry (μPIV), described in detail e.g., by Santiago et al.[20] or by Meinhart et al.[21] In contrast to the measurement of the concentration field, fluorescent microspheres are suspended for that purpose in the water of one syringe pump. The microspheres, obtained from *Duke Scientific Cooperation*, have a diameter of $d_p = 500\ nm$. These particles are made of polystyrene which has a density of $\rho_p = 1050\ kg/m^3$. The diffusion coefficient of these particles is of order $\sim 10^{-13}\ m^2/s$.

To allow for an estimation of the influence of buoyant forces, we introduce the Archimedes number

$$Ar = \frac{(\rho - \rho_p) g d_p^3}{\rho \nu^2} \tag{1}$$

Here, ρ is the density, and ν is the kinematic viscosity of the liquid; g denotes gravitational acceleration. The Archimedes number represents the ratio of buoyant and viscous forces, acting at the particles. We find $Ar \simeq 10^{-8} \ll 1$ and conclude that buoyant forces should not have an appreciable effect onto the particles. Following Crowe et al.[22] the Stokes number provides another helpful means to characterize the movement of particles within flows. The Stokes number for the present situation is given by

$$St = \frac{\tau_p}{\tau_f} = \frac{d_p^2 \rho_p u_0}{18 \nu \rho d_0} \tag{2}$$

Here $\tau_p = \rho_p d_p^2 / 18\mu$ is the response time scale of the particles (due to drag and Stokes flow) and $\tau_f = d_0/u_0$ is the time scale of the flow. Whereas u_0 denotes the mean axial velocity in the channel, and μ the dynamic viscosity of the liquid. Hence, the Stokes numbers allows to judge, whether the particles can follow the flow. Typical Stokes numbers within our experiments are of the order $St \simeq 10^{-4} \ll 1$. From this it can be concluded that the microspheres have ample of time to follow any change of velocity within the flow. In summary, both the Archimedes number and the Stokes number clearly indicate that the particles should perfectly follow the flow.

Two Nd:YAG lasers (*Solo-PIV, New Wave Inc.*) are used as light sources providing two consecutive pulses of green light of wave length $\lambda = 532\ nm$. The light, guided through the optical devices and the microscope objective (magnification $10\times$), illuminates the measuring volume within the channel. The microspheres are customized for emission within the red regime, i.e., at a wave length around $\lambda = 612\ nm$. An image of the particle distribution is captured by the CCD camera at each laser pulse. The images are subdivided into so–called interrogation areas. We select a size of 16×16 *pixels*, and 50% overlap for an interrogation area. The displacement of the particles within an interrogation area is determined by a comparison of two consecutive images by means of statistical methods (cross correlation). The displacement vectors in conjunction with the time between two images then allows to infer the local velocity field. Only particles within the focal plane of the microscope are imaged in sharp fashion and, moreover, at high fluorescence intensity by the CCD camera. The other particles remain unfocused and have little intensity, contributing essentially to the background noise. In contrast to the conventional PIV method, with the thickness of the light sheet defining the measuring volume, in μPIV the properties of the imaging system determine the thickness of the measuring volume. Following Meinhart et al.[21] the thickness of the measuring volume is given by the so–called depth of correlation, which for our parameters can be estimated to $\delta_z \simeq 10\ \mu m$. The μPIV method allows for the determination of two velocity components, the third component, in the direction of the microscope axis, cannot be captured. Moreover, both velocity components are averaged over the depth of correlation. Nevertheless, the two components of the velocity vector can be measured across the complete channel cross-section by shifting the focal plane along the microscopic axis.

If only one syringe pump is charged with seeded liquid, the partial (velocity) measurements give, moreover, valuable information on the (virtual) contact interface: the seeded and the unseeded liquid streams merge in the Y-junction, and enter the twice–folded channel segment in a layered fashion. Consequently, the contact interface can be found between seeded and unseeded portion of the liquid. This procedure, hence, does not only provide partial velocity profiles, but also allows to follow the evolution of the contact interface along the twice–folded channel segment. An evaluation of the secondary–flow effects, caused by the folded geometry, contributing to mixing or reaction zone enhancement, then appears possible by the distortion of the contact interface. Moreover, this partial seeding can perfectly be reproduced by numerical simulations. Unlike solving the mass transport equation, with the common problems due to numerical diffusion, numerical particle tracking is free of diffusion.

Simulation methodology

In this work the aim is to compare experiments with numerical simulations. Hence, the governing equations have to be identified and adequate boundary conditions have to be chosen. Further, the details of the computational domain and of the numerical procedure are described within this chapter.

Governing equations

To model the pressure–driven base flow, we rely on the standard Navier–Stokes equations. Since we expect secondary flows, the 3-D equations are necessary. Hence, the governing equations for a time–dependent flow of an incompressible Newtonian fluid are

$$\nabla \cdot \vec{v} = 0 \tag{3}$$

$$\rho \left[\frac{\partial \vec{v}}{\partial t} + (\vec{v} \cdot \nabla) \vec{v} \right] = -\nabla p + \mu \Delta \vec{v} \tag{4}$$

Here, $\vec{v}$ represents the velocity vector, and t time, μ is the dynamic viscosity, and p is pressure. The concentration field of the fluorescence dye is simulated by means of a standard convection–diffusion equation, namely by

$$\frac{\partial c}{\partial t} + \nabla \cdot (\vec{v} c) = D \Delta c \tag{5}$$

In Eq. 5, c denotes the concentration, and D is the binary diffusion coefficient. However, the discretization of the con-

vective term in Eq. 5 usually creates numerical diffusion, which may substantially add to physical diffusion.[23] Numerical diffusion in the mass transport equation appears due to large $|\vec{v}|/D$, which would require an (unfeasible) extremely–fine mesh. Instead, the mesh is chosen to resolve the flow Eqs. 3–4 adequately. Therefore, it can be expected that the computed concentration fields differ noticeably from the experimental concentration fields. Numerical simulations of diffusion–free mass transport, on the other hand, are possible on the basis of particle tracking, which is likewise part of our investigations.

The velocity of a single particle i corresponds to the derivative of its position vector with respect to time, i.e.

$$\vec{v}_{P,i} = \frac{\partial \vec{x}_{P,i}}{\partial t} \tag{6}$$

We consider the (numerical) particle to be free of mass, i.e., free of inertia. Further, the (numerical) particle has a vanishing diameter, and, hence, does not disturb the flow. It has been shown by means of the Archimedes number and Stokes number (cf. Eqs. 1, 2) that the experimental particles also follow the flow in an (almost) ideal manner. The particle velocity is then determined by the velocity field of the liquid and the particle trajectory can be obtained from integration, i.e.

$$\vec{x}_{P,i} = \int_0^t \vec{v} dt + \vec{x}_{P,i}(t=0) \tag{7}$$

A comparison of the computed concentration field, and the particle distribution allows to qualitatively judge on the influence of diffusion. Further, the contact interfaces from numerical particle tracking, and from experimental partial particle tracking can be compared to obtain more insight into the transport processes.

A nondimensionalization of Eqs. 3–7 is advantageous in many respects, e.g., we can solve an entire class of problems. Hence, we introduce a homogenous (channel) length scale, a homogenous velocity scale, a (convective) transport time scale, a (viscous) pressure scale, and a concentration scale, namely

$$\vec{X} = \frac{\vec{x}}{d_0}, \quad \vec{V} = \frac{\vec{v}}{u_0}, \quad T = \frac{t u_0}{d_0}, \quad P = \frac{p d_0}{\mu u_0}, \quad C = \frac{c}{c_0} \tag{8}$$

Within the scaling (8) c_0 denotes the preparation concentration of the dye. After the introduction of these scales we obtain the dimensionless version of the governing equations as

$$\nabla \cdot \vec{V} = 0 \tag{9}$$

$$Re\left[\frac{\partial \vec{V}}{\partial T} + (\vec{V} \cdot \nabla)\vec{V}\right] = -\nabla P + \Delta \vec{V} \tag{10}$$

$$\frac{\partial C}{\partial T} + \nabla \cdot (\vec{V} C) = \frac{1}{ReSc} \Delta C \tag{11}$$

$$\vec{X}_{P,i} = \int_0^T \vec{V} dT + \vec{X}_{P,i}(X=0) \tag{12}$$

Within Eqs. 9–12 the dimensionless Reynolds number Re, and Schmidt number Sc arise, which are defined by

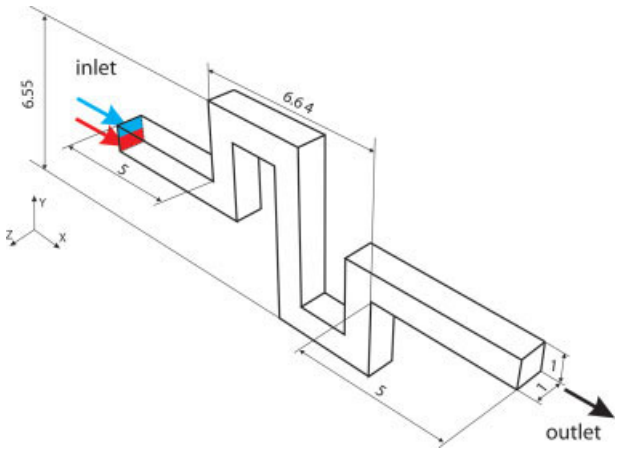

Figure 3. Computational domain.

[Color figure can be viewed in the online issue, which is available at www.interscience.wiley.com.]

$$Re = \frac{u_0 d_0}{\nu}, \quad Sc = \frac{\nu}{D} \tag{13}$$

The Dean number does formally not appear within a cartesian coordinate system. Furthermore, the investigated folded microchannel consists of sharply–folded bends, and, hence, an average radius of curvature, necessary to determine the Dean number, is not obvious. To obtain an estimation of the Dean number within this sharply–folded bend, we engage a comparable smoothly–curved bend. This smoothly–curved bend features identical square cross section and identical volume as the sharply–folded bend (cf. Figure 3). From this, the mean radius of curvature can be calculated to be $r_0 \simeq 195\ \mu m$ and the Dean number within the sharply–folded bend can be estimated as

$$De = \sqrt{d_0/r_0} Re \simeq 3/4 Re \tag{14}$$

Computational procedure

To obtain a reasonable computation time, the computational domain is limited to the twice–folded microchannel as sketched in Figure 3. This computational domain is cut out of the complete micromixer geometry in a distance of five channel widths upstream of the first and downstream of the last bend, respectively. At all walls we employ the no–slip condition, i.e.

$$\vec{V}_{wall} = 0 \tag{15}$$

With respect to the long straight inlet and outlet channel segments, the assumption of a fully–developed flow profile appears justified. Hence

$$V = W = 0 \tag{16}$$

is used as boundary condition at the inlet and at the outlet cross section. The inlet profile $U(Y_0, Z_0)$, moreover, can be taken from an analytical series solution (cf. Ward-Smith[24]) for a square channel to be

$$U(Y,Z) = -\frac{1}{2}\frac{dP}{dX}\left[\frac{1}{4} - Y^2 - 4\sum_{n=0}^{\infty}\frac{(-1)^n}{((2n+1)\pi)^3} \times \frac{\cosh((2n+1)\pi Z)}{\cosh((2n+1)\pi/2)}\cos((2n+1)\pi Y)\right] \quad (17)$$

Thus, we have to employ

$$\frac{\partial U}{\partial X} = 0 \quad (18)$$

at the outlet cross section. To mimic the experiments, we must enable the merging of the fluorescence dye mixture and the pure water. Since the upstream Y-junction is not part of the computational domain, we adapt the boundary condition at the inlet cross-section instead. At the lower half of the inlet cross section we implement a concentration of $C = 1$, while at the upper half $C = 0$ is used. All other properties of the liquid, i.e., density and viscosity, remain exactly the same. At the outlet cross section and the wall a vanishing flux is used as boundary condition, i.e.

$$\frac{\partial C}{\partial \vec{n}} = 0 \quad (19)$$

Here, $\vec{n}$ is the vector normally directed to the specific domain. The seeding of the particles corresponds to the employed concentration boundary conditions.

All simulations were performed with the commercial finite–element–method (FEM) code *FIDAP 8.7.2*. For the spatial discretization we engage 27–node quadratic elements, featuring triquadratic interpolation functions, proving to be second–order accurate. Overall, the entire simulated geometry includes about $1.2 \cdot 10^6$ nodes. The time step is discretized by using an implicit second–order predictor/corrector scheme (explicit Adams–Bashford/stable trapezoidal rule). The velocity–pressure coupling is realized by a penalty function approach. Element sizes and the size of the time step are chosen in such a way that the solution has converged at all time steps, so that the RMS of the residuum, summed-up over all equations, remains smaller than $1 \cdot 10^{-4}$. The particle trajectories are integrated by a second–order Runge–Kutta integration scheme.

Results

Measurements and computations are performed at Reynolds numbers of $Re = 27$ and $Re = 42$, corresponding to average axial velocities of $u_0 = 0.245$ *m/s* and $u_0 = 0.382$ *m/s*, respectively. According to Eq. 14 we estimate Dean numbers of $De \simeq 20$ and $De \simeq 32$. Given these moderate Reynolds (Dean) numbers, the secondary flow is limited to one pair of counter–rotating vortices. The investigation of flows with higher velocities, however, is not relevant for lab on a chip microflows. The diffusion coefficient of *Rhodamine B* in water is $D = 4.27 \cdot 10^{-10}$ m^2/s.[25] In conjunction with a density of $\rho = 1{,}000$ kg/m^3, and a dynamic viscosity of $\mu = 1 \cdot 10^{-3}$ *Pas* of the solvent water, a Schmidt number of $Sc \simeq 2340$ is estimated. The simulation of systems with such large Schmidt numbers leads to numerical instabilities (spatial oscillations) within the solution of the concentration field due to limited mesh refinement capabilities. Hence, we limit the Schmidt number to $Sc = 100$, corresponding to a diffusion coefficient of $D = 1 \cdot 10^{-8}$ m^2/s, to obtain stable numerical solutions for the concentration field. These solutions, therefore, will suffer from strong diffusion, if compared to the experimental situation.

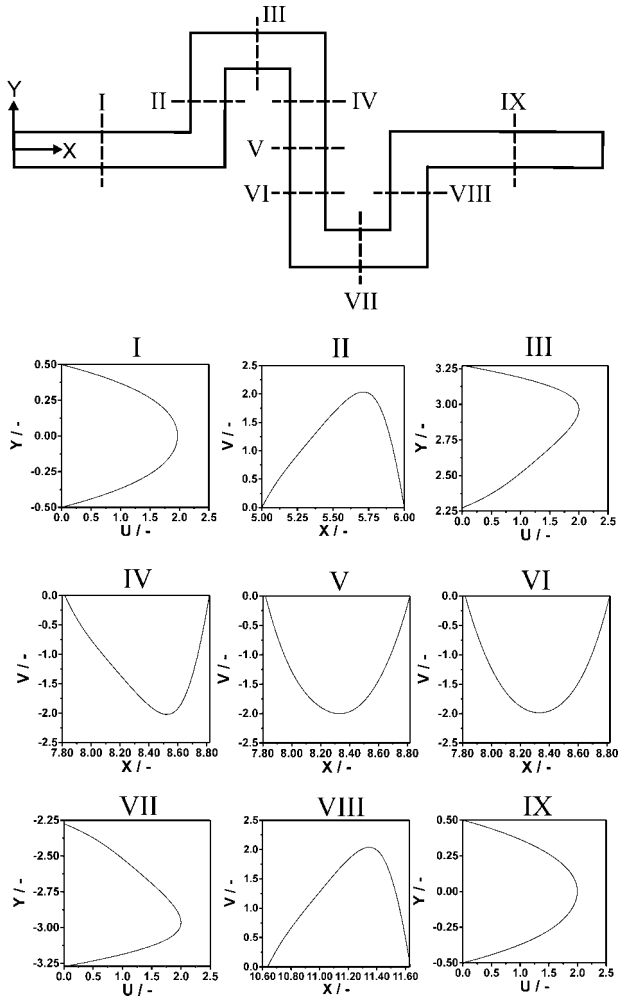

Figure 4. Axial velocity profiles within the midplane (Z = 0) at various positions of the folded microchannel.

The simulation is performed at $Re = 42$.

We shall mainly concentrate on the results for $Re = 42$, the flow at $Re = 27$ exhibits weak secondary flow only. Figure 4 shows axial velocity profiles within the midplane (Z = 0) at various positions I–IX of the folded microchannel. The numerical simulation indicates secondary flows at certain positions within the meander. In the middle of the first straight channel segment (position I), we recognize an ordinary laminar flow indicated by the corresponding symmetric velocity profile. After the first bend at position II the velocity profile is nonsymmetric; the maximum of the velocity is shifted to the right (outer) channel wall. Obviously, this is a result of centrifugal forces acting in the first bend and transferring momentum perpendicular to the main flow towards the outer wall. In the second bend, the centrifugal forces are

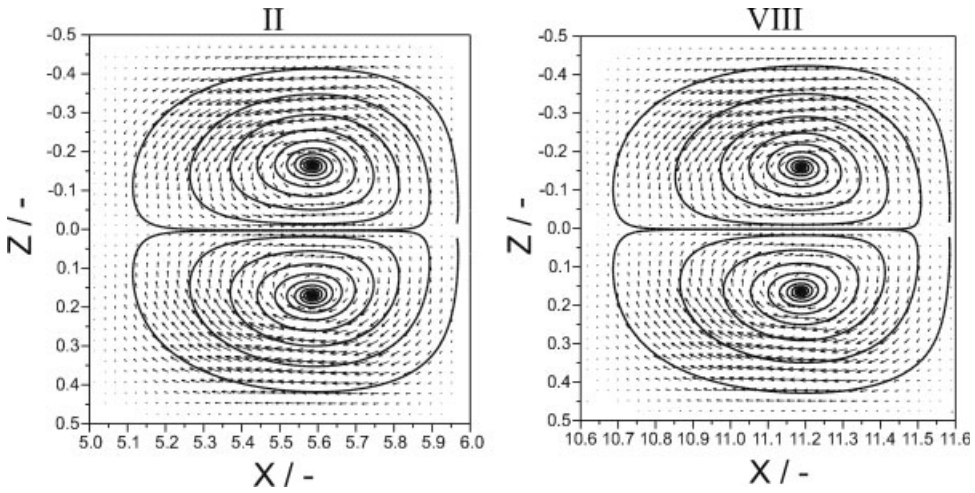

Figure 5. Secondary velocity vector field and particle trajectories within the cross sections at position II and VIII for *Re* = 42.

in the opposite direction, and, hence, the velocity peak at position III is shifted toward the opposite (left) channel wall. At position IV the influence of the centrifugal forces is still present, as can be inferred from the outward displacement of the velocity maximum. As we follow the flow downstream to position V, the influence of centrifugal forces has vanished and the symmetric velocity profile is restored; this also holds for position VI. In other words, the secondary flow decays along the straight channel segment. Following the further bends of the channel, at positions VII and VIII we again see shifted velocity maxima, and, hence, indications of secondary flows. The profile within the last straight channel segment at position IX is again of symmetric shape. It is remarkable that all shifted velocity profiles appear identical, regardless of whether the flow has passed through one bend, two, or even more bends in sequence. It appears that the last bend of a sequence shapes the velocity profile downstream. This can likewise be confirmed by inspecting the secondary velocity maps, taken e.g., in cross sections II and VIII and plotted in Figure 5. The velocity vectors within cross-section II clearly indicate the presence of two counter–rotating (Dean) vortices. The velocity vectors within the center of the cross-section are directed outwards, while along the channel walls a recirculation is established. The secondary flow vectors are obtained from the complete velocity vector without axial component. We superpose two (virtual) particle trajectories in each cross section of Figure 5 for clarity. These particle trajectories have been obtained from integration, based on the secondary flow field. The secondary flow field within cross section VIII appears almost identical to cross-section II. However, the upstream conditions are different for both cross sections II and VIII. The flow at position II has passed through one bend, while the flow at position VIII, starting from a symmetric profile at position VI, has passed through two bends. The secondary flow characteristics, therefore, appears little affected by the number of bends.

Height–averaged concentration fields within the microchannel, measured by the μLIF method, are presented in Figure 6, where (a) shows the result for $Re = 27$, and (b) shows the result for $Re = 42$. In Figure 6a we basically recognize three layers of liquid. The lower layer is at intensities around 100%, corresponding to $c_0 = 0.21\ g/dm^3$ or $C = 1$; the upper layer is at intensities around 0% ($C = 0$) and, further, a concentration boundary layer can be recognized between the

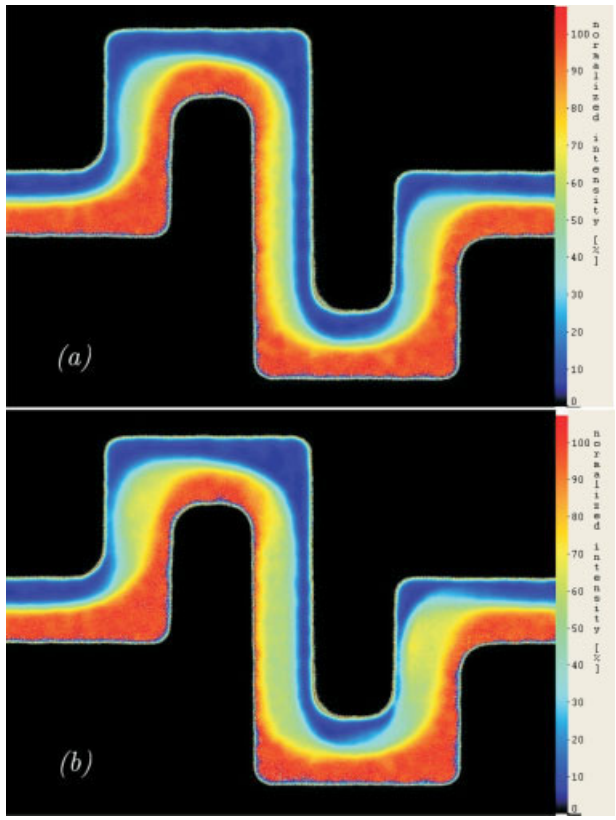

Figure 6. Measured height–averaged concentration fields within the folded microchannel at (*a*) *Re* = 27, and (*b*) *Re* = 42.

[Color figure can be viewed in the online issue, which is available at www.interscience.wiley.com.]

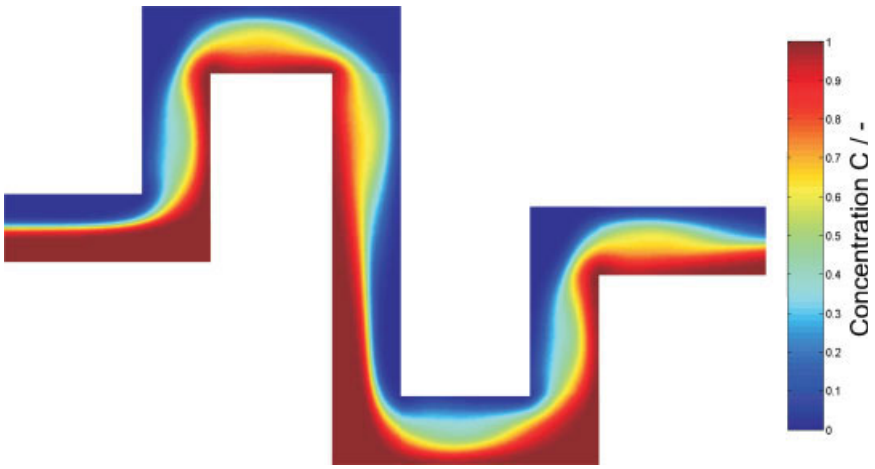

Figure 7. Simulated height–averaged concentration field at *Re* = 42.

[Color figure can be viewed in the online issue, which is available at www.interscience.wiley.com.]

upper and the lower layer. The concentration boundary layer is relatively thin at all horizontal segments of the folded microchannel. Within the vertical segments, however, the layer appears wider, indicating the effect of the secondary flow onto the mixing. In Figure 6b a similar concentration pattern is found, but the secondary–flow mixing appears more pronounced. Especially in the middle vertical microchannel segment, an almost homogenously–mixed region can be found. For relatively–large Reynolds numbers, diffusion in the upstream common channel does not have enough time to achieve significant mixing. This conclusion can be drawn e.g., from the measurements of Matsumoto et al.[18] Thus, at lower Reynolds numbers a thicker concentration boundary layer can be expected due to a larger residence time. For the interpretation of these concentration fields, however, we have to keep in mind that the experimental method provides only height–averaged concentration fields. Secondary flows, induced at bends, are responsible for concentration variations along the optical path (channel height), which then may lead to apparently–mixed regions.

We now compare the experiments against the results of the simulation for $Re = 42$, given in Figure 7. The presented concentration field is height-averaged in a similar manner as in the experiments. We find a qualitative agreement with minor discrepancies. The concentration boundary layers within the vertical channel segments appear likewise wider, but the widening in the middle vertical channel is not present along the complete length. Moreover, the concentration boundary layer appears wider also within parts of the horizontal segments. This cannot be recognized within the experimental data (cf. Figure 6b). The differences between simulation and experiment could be related to diffusion. In the simulations we have on one hand numerical diffusion and on the other hand an unphysically–large diffusion coefficient to mitigate the numerical oscillations. This results in diffusion, which is substantially stronger than the true diffusion of *Rhodamine B* in water. The differences could also be related to different flow fields. Slightly–different flow fields may arise, since the experimental microchannel features rounded corners, while the simulations feature sharp corners (cf. Figures 6 and 7).

To clarify the effect of diffusion, we apply partial seeding both experimentally and numerically, as described in section velocity field. Experimentally, the seeding of the lower inflow with microspheres enables us to follow the seeded stream through the microchannel and to obtain velocity information for this stream. The unseeded upper inflow and its stream, of course, does not provide any velocity information. We measure the particle and velocity field within 17 levels from the bottom to the top of the microchannel. Hereby, we observe that the area of the microchannel occupied by the seeding particles changes from level to level, demonstrating the 3-D character of the flow. Figure 8a shows an example for such a measured particle and velocity field at a level 40 μm above the bottom wall of the microchannel ($Z = -0.145$). Numerically, we bring approximately 1,100 particles into the lower half of the folded microchannel and integrate their paths. At all positions, where we find particles, e.g., around the level $Z = -0.145$, we plot the velocity vectors and, hence, obtain an analogous image of the particle and velocity field, comparable to the experimental findings. The result of this numerical procedure is shown in Figure 8b also for the level $Z = -0.145$. It should be noted that the particle and velocity information from the experiments is collected across about 10 μm in depth, while within the simulations spacing of the mesh leads to a range of 4 μm. This certainly leads to different particle densities from both methods. Within both figures the velocity vectors are, moreover, color–coded to allow for immediate comparison, whereas the dimensional value of $u = 0.7$ m/s within the experimental data corresponds to the dimensionless value of $V = 1.8$ within the theoretical data.

We see from the numerical image (cf. Figure 8b) that, even though the inflow is strictly layered, the secondary flow leads to a deflection of the seeded stream across the complete cross section at the very outlet. The effect of the Dean vortices appears particularly strong downstream of each bend. Comparing the theoretical particle distribution to the experimental particle distribution (cf. Figure 8a) reveals qualitative agreement. However, the seeded stream appears wider within the experimental image, which is due to a larger mean particle concentration. This is not surprising, since the theoretical

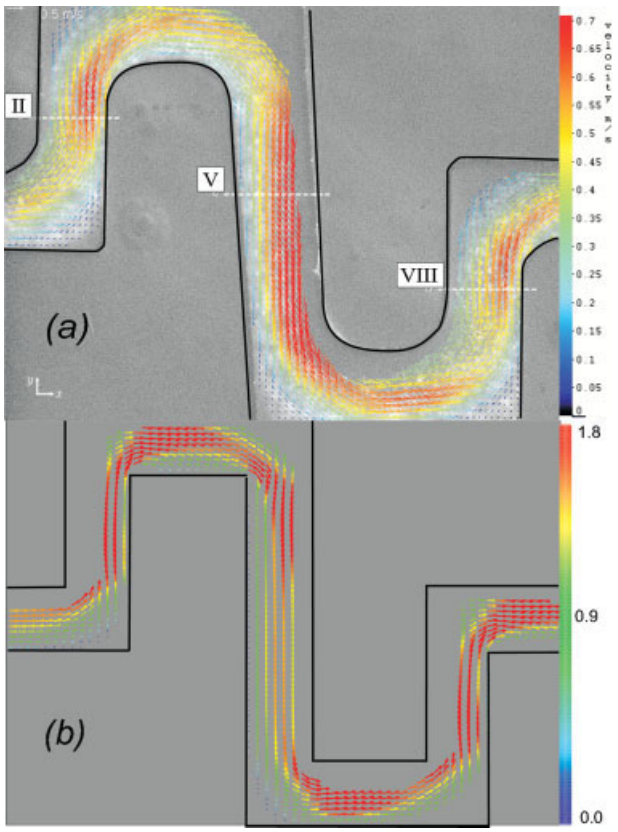

Figure 8. Measured *(a)* and simulated *(b)* velocity field for *Re* = 42 at a level 40 μm ($Z = -0.145$) above the channel bottom.

[Color figure can be viewed in the online issue, which is available at www.interscience.wiley.com.]

image relies on local information, while the experimental image involves substantial height–averaging in each level. It can, therefore, be expected that the theoretical image shows a sharp transition from the seeded to the unseeded stream, while the experimental image features a smeared transition. The comparison of the regions of large velocities (yellow/red arrows) certainly shows good agreement, all characteristic features are present in both images. Particularly, after each bend the velocity maxima are shifted outwards in both images. Again, the numerical results reflect local (dimensionless) velocities, while the μPIV method averages likewise the (dimensional) velocity data across layers of about 10 μm thickness. Moreover, we need to recall that the real channel geometry, featuring several rounded corners, does differ from the simulation geometry, where for simplicity sharp corners have been implemented. Finally, the merging of both inlet flows at the Y–mixer and the flow downstream to the meander is not simulated numerically. Instead, an idealized concentration boundary condition is formulated at the inlet cross section for the simulations. Given all these differences, the overall agreement is acceptable.

In a next step, we collect (partial) profiles of the axial velocity at all height–levels to obtain a three–dimensional insight. The results are presented in Figure 9 for the cross sections II, V and VIII (cf. Figure 4), i.e., within all vertical channel segments. The first column gives the measured (partial) axial velocity fields, the second column gives the corresponding simulated fields. The effect of the secondary flow onto the profile at position II can be recognized from two features: (1) The unseeded liquid in the channel center has penetrated into the seeded liquid, which in turn has penetrated into the unseeded liquid along both channel walls. This is due to the pair of counter–rotating vortices (cf. Figure 5). (2) The velocity maximum is shifted from the center into the outward direction. The area adjacent to the inner wall ($X = 5$), and the adjacent penetration finger is occupied by unseeded liquid, and, hence, provides no velocity information. Within the middle of the long vertical channel (position V) the velocity profile is different. Here, the penetration finger consists of seeded liquid, penetrating into unseeded liquid in the channel center. The seeded stream occupies the inner part of the cross section through two bends, which is opposite to the situation after the first bend (cross section II). Hence, the pattern in cross section II appears reversed and even developed further to the complementary pattern, visible at cross section V. The profile at cross section VIII, finally, is similar to the profile at cross section II. Again, this similarity is surprising, not only with respect to the flow, but also to the distribution of seeded and unseeded liquid, since upstream conditions for both cross sections are different.

The comparison of experimental and simulated profiles reveals reasonably–good agreement with regard to both velocity amplitudes and shapes of the profiles. As expected, the penetration pattern and velocity profile at the seeded/unseeded transition appears sharp within the simulations and smeared within the experiments, due to the spatial averaging within the measuring technique. Additionally, we find minor discrepancies with regard to the penetration of both liquids into each other: this penetration appears more pronounced in the simulations. At position V another discrepancy arises from the place of the velocity maxima. The measured velocity maximum is found outside of the channel center, while it is in the center within the simulations. This indicates a slightly–faster decay of centrifugal effects along straight segments within the simulations. This faster decay can only be attributed to different flow fields in experiment and simulation. Again, the slight differences in geometry (rounded/sharp corners) can lead to different streamline curvature in experiment and simulation.

The distributions of the seeded and non–seeded liquid at cross sections II, V and VIII are directly imaged in Figure 10 without the velocity information. Within the left column we see results from numerical simulations of the concentration field, obtained for the unphysically–large diffusion coefficient. The middle column shows the distribution of seeded and unseeded liquid as result of numerical particle tracking. This method should provide theoretical results without diffusion. The right column gives the experimental distribution, i.e., the areas in which consistent velocity information is obtained experimentally. Such areas are obviously characterized by the presence of (sufficient) seeding particles.

With regard to the middle and right columns, these particle distributions are already present in Figure 9. Hence, we recover all characteristics of these particle distributions, without the difficulties related to the perspective view and to regions, hidden by the velocity profiles. There is no need to

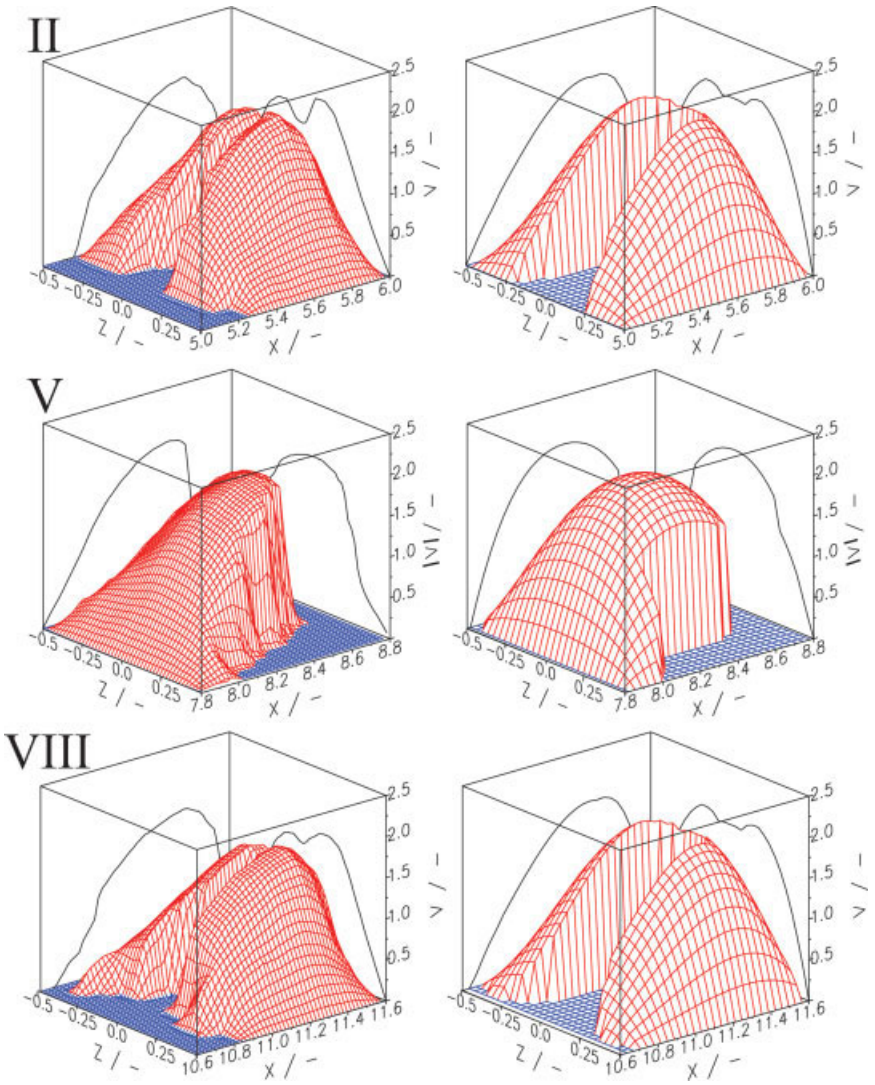

Figure 9. (Partial) velocity fields at cross sections II, V, and VIII for *Re* = 42. The left column is obtained from experiments, the right column is obtained from simulations.

[Color figure can be viewed in the online issue, which is available at www.interscience.wiley.com.]

discuss these characteristics again. Additionally, the effect of diffusion can be accessed from a comparison of the particle distributions in the left and middle column. The numerical particle tracking (middle column) reveals a sharp transition from seeded to unseeded liquid. The simulation of the concentration fields (left column) reveals in contrast a pronounced concentration boundary layer between both liquids. The general shapes of both theoretical distributions, though, appear similar. Differences are present particularly with regard to both length and width of the penetration fingers. The length of the penetration finger, obviously, is reduced with increasing diffusion; the width of the penetration finger is increased with increasing diffusion. We have to recall that both results in the left and middle column are based exactly on the same velocity field. Further, the (numerical) particles follow the flow in an ideal manner without any disturbance to the flow. Given identical flow fields, the differences can only be attributed to differences in diffusion.

To obtain a quantitative measure, we have extracted the fraction α of the cross section occupied by the seeded liquid, according to

$$\alpha = \frac{A}{A_0} \tag{20}$$

Here A is the area occupied by the seeded liquid, and A_0 is the entire cross–sectional area. The results are summarized in Table 1. For cross sections II and VIII the fractions α from numerical particle tracking (b) agree reasonably with the fractions from experimental particle tracking (c). This agreement remains remarkable, as we already discussed the differences in spatial averaging between the theoretical and experimental methods. At cross section V this agreement, however, is not as good. At cross section V the fraction α from the simulation of the concentration field (a) appears to agree better with the experimental findings (c).

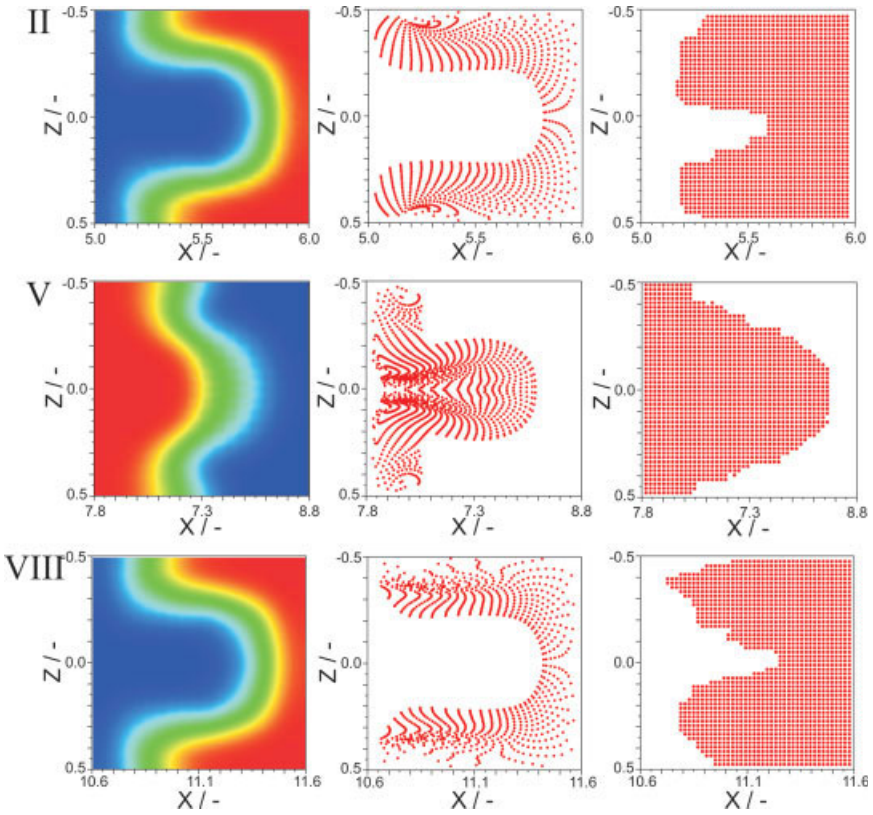

Figure 10. Cross–sectional distribution of seeded and unseeded liquid at cross sections II, V, and VIII for *Re* = 42.

The left column is obtained from simulation of the concentration field (with diffusion), the middle column from the simulated particle distribution (without diffusion), the right column from experiment. [Color figure can be viewed in the online issue, which is available at www.interscience.wiley.com.]

The contact interface of both liquids certainly would be the site of chemical reactions. Hence, increasing the contact interface by means of e.g., the secondary flow is essential to improve the yield of such reactions. Consequently, we have further calculated the projected length of the concentration boundary layer (case a) and the projected length of the contact interface (cases b,c) in all cross sections. Table 2 gives the ratios of these lengths to the projected lengths of the undistorted contact interfaces. The more this ratio departs from unity, the greater is the increase of the contact interface. It should be mentioned, though, that by evaluating the cross sections II, V, and VIII we can only obtain partial information on the 3-D contact interface. For case (a), the projected length of the concentration boundary layer is taken from isoconcentration line of $C = 0.01$. The ratios obtained from numerical and experimental particle tracking (cases b,c) agree to a reasonable degree, while the ratios from the numerical simulation of the concentration field (case a) are generally lower. Overall, an increase of the projected length of the contact interface by a factor of around 2 is found. As the distortion of the contact interface in the axial direction appears minor, this factor of 2 should be a good estimate likewise for the contact interfacial area.

Summary and outlook

In the present article, we investigate the flow and mass transport within a twice–folded microchannel, serving as essential part of an electrically–excited micromixer. At this point, we concentrate on the pure pressure–driven flow without electrical excitation. Even for a pure pressure–driven flow through a meander we can expect a secondary flow, which can be beneficial for mixing and for the progress of chemical reactions. Hence, experiments and numerical simu-

Table 1. Cross–Sectional Fraction α at Positions II, V and VIII According to (a) Numerical Simulation of the Concentration field, (b) Numerical, and (c) Experimental Particle Tracking for *Re* = 42

–	II	V	VIII
a)	0.59	0.62	0.59
b)	0.66	0.49	0.63
c)	0.71	0.64	0.71

Table 2. Increase of the Projected Length of the Contact Interface at Cross Sections II, V and VIII, According to (a) Numerical Simulation of the Concentration Field, (b) Numerical, and (c) Experimental Particle Tracking

–	II	V	VIII
a)	1.66	1.36	1.65
b)	2.01	1.87	1.98
c)	1.84	1.77	1.91

lations at Reynolds numbers of $Re = 27$ and $Re = 42$ are performed and compared carefully.

The experimental investigations of the concentration field are based on a laser–induced fluorescence method (μLIF). We mark one part of the flow by a fluorescent dye and illuminate the microchannel measuring volume by laser light. The intensity of the recorded fluorescence light for this setup is linked to the height–averaged concentration of the dye. We find that the concentration fields exhibit mixed regions, which appear more pronounced at the higher Reynolds number flow. Assisted by numerical simulations we identify secondary flows, induced at the bends, which are responsible for concentration variations along the channel height. Since the measuring technique provides height–averaged concentrations only, we conclude that these mixed regions are only apparently mixed. A detailed comparison of experimental findings on the height–averaged concentration field and corresponding numerical results shows reasonable agreement. Minor discrepancies can be attributed to the unphysically–large diffusion coefficient, used within the numerical simulations to prevent instabilities of the numerical scheme.

Experimentally, the velocity field is captured by the micro particle image velocimetry (μPIV). We deviate from standard μPIV by seeding a partial stream only. This leads to regions with and regions without particles. Even though we obtain velocity information only from seeded regions, by this method we can follow the evolution of the (virtual) contact interface between seeded and unseeded liquid through the microchannel. Moreover, this method reveals, to good approximation, the pure convective mass transport, and, hence, provides "diffusion-free" contact interfaces. It can further be perfectly imitated by numerical particle tracking simulations. We compare measurements and simulations of these partial velocity fields at certain height levels of the microchannel. There is good agreement both with regard to the seeded regions, and with regard to the velocity amplitudes. We further take all velocity data, measured at different height levels, to construct the 3-D (partial) profile of the axial velocity within the complete cross section. The results clarify that the secondary flow is responsible for the penetration of seeded and unseeded liquids into each other. The profiles at selected channel segments are compared to corresponding profiles from numerical simulations and reasonably–good agreement is found. Finally, we work out how the obtained contact interface differs, depending on whether it is obtained (1) from numerical simulations of the mass transport equation (with diffusion), (2) from numerical particle tracking (without diffusion), (3) or from experimental particle tracking. The comparison of both numerical results clarifies the effect of diffusion. The length of the projected contact interface and the fraction of the seeded flow, both within a cross section, are engaged to allow for a quantitative comparison. The length of the projected contact interface after bends is found to be typically stretched by a factor of two. The agreement for both quantities is best between numerical and experimental particle tracking.

The investigation of the pressure–driven flow within the twice–folded microchannel shows that the combination of μPIV and μLIF is an excellent tool, which allows to access both 3-D profiles of the axial velocity and height–averaged concentration fields. The experimental partial particle tracking provides additional insight into the mass transport and is useful for the correct interpretation of the height–averaged concentration fields from μLIF. The potential of these methods appears to be comparable to confocal fluorescence microscopy, but is achieved at much lower costs. Moreover, particle tracking can be validated by corresponding numerical simulations, without the problems associated with numerical diffusion. The evolution of the contact interface between both liquids, the secondary flow, and the consequences for the height–averaged concentration fields can be perfectly understood from the above combined information. The comparison of experimental and numerical results overall shows reasonably–good agreement, discrepancies can be attributed to differences in averaging ranges, to differences in the geometric details of the microchannels, and to the limited domain (and corresponding boundary conditions), simulated numerically.

With respect to future research, there are obvious extensions towards the electrically–excited flow within this micromixer. Open questions comprise whether the earlier experimental methods are capable to resolve more complex flow fields or concentration fields with a higher degree of mixing. Certainly, e.g., the μPIV method will not resolve the velocity profile across an electrical double layer (EDL) of some ten nanometer thickness. Likewise, the height–averaged concentration fields from μLIF will only allow for limited conclusions with regard to complex 3-D concentration fields. Finally, it remains interesting to learn whether the partial particle tracking is capable to resolve highly–distorted contact interfaces.

Literature Cited

1. Henning T, Brandner JJ, Schubert K. Characterization of electrically powered micro heat exchangers. *Chem Eng J*. 2004;101:339–345.
2. Ehrfeld W, Hessel V, Löwe H. *Microreactors: new technology for modern chemistry*. Weinheim: Wiley-VCH 2000.
3. Manz A, Graber N, Widmer HM. Miniaturized total chemical analysis systems: a novel concept for chemical sensing. *Sens Actuators B*. 1990;1:244–248.
4. Ramsey JM. The burgeoning power of the shrinking laboratory. *Nature Biotech*. 1999;17:1061–1062.
5. Kakuta M, Bessoth F, Manz A. Microfabricated devices for fluid mixing and their applications for chemical synthesis. *Chem Record*. 2001;1:395–405.
6. Meisel I, Ehrhard P. Electrically-excited (electroosmotic) flows in microchannels for mixing applications. *Eur J Mech B/Fluids*. 2006; 25:491–504.
7. Dean WR. Note on the motion of fluid in a curved pipe. *Phil Mag*. 1927;4:208–223.
8. Dean WR. The stream-line motion of fluid in a curved pipe. *Phil Mag*. 1928;5:673–695.
9. Joseph B, Smith EP, Adler RJ. Numerical treatment of laminar flow in helically coiled tubes of square cross section. part I. stationary helically coiled tubes. *AIChE J*. 1975;21:1298–1302.
10. Cheng KC, Lin R-C, Ou J-W. Fully developed laminar flow in curved rectangular channels. *J Fluids Eng*. 1976;41:41–48.
11. Ghia KN, Sokhey JS. Laminar incompressible viscous flow in curved ducts of regular cross sections. *J Fluids Eng*. 1977;99:640–648.
12. Hille P, Vehrenkamp R, Schulz-Dubois EO. The developement and structure of primary and secondary flow in a curved square duct. *J Fluid Mech*. 1985;151:219–241.
13. Schönfeld F, Hardt S. Simulation of helical flows in microchannels. *AIChE J*. 2004;50:771–776.

14. Yamaguchi Y, Takagi F, Yamashita K, et al. 3-D simulation and visualization of laminar flow in a microchannel with hair-pin curves. *AIChE J*. 2004;50:1530–1535.
15. Kenis PJA, Ismagilov RF, Whitesides GM. Microfabrication inside capillaries using multiphase laminar flow patterning. *Science*. 1999;285:83–85.
16. Hisamoto H, Saito T, Tokeshi M, Hibara A, Kitamori T. Fast and high conversion phase-transfer synthesis exploiting the liquid-liquid interface formed in a microchannel chip. *Chem Com*. 2001;24:2662–2663.
17. Freitag A, Dietrich T, Scholz R. Glass as material for microreaction technology. in *Proc of the 4th Int Conf on Microreaction Technology, IMRET 4*(Atlanta, USA):48–54, 2000.
18. Matsumoto R, Farangis Zadeh H, Ehrhard P. Quantitative measurement of depth averaged concentration fields in microchannels by means of a fluorescence intensity method. *Exp Fluids*. 2005;39:722–729.
19. Sakakibara J, Adrian R. Whole field measurement of temperature in water using two-colour laser induced fluorescence. *Exp Fluids*. 1999;6:7–15.
20. Santiago JG, Wereley ST, Meinhart CD, Beebe R, Adrian RJ. A particle image velocimetry system for microfluidics. *Exp Fluids*. 1998; 25:316–319.
21. Meinhart CD, Wereley ST, Santiago JG. PIV measurements of a microchannel flow. *Exp Fluids*. 1999;27:414–419.
22. Crowe C, Sommerfeld M, Yutaka T. *Multiphase flows with droplets and particles*. Boca Raton: CRC Press; 1998.
23. Ferziger JH, Peric M. *Computational Methods for fluid dynamics*. Berlin, Heidelberg, New York: Springer; 1996.
24. Ward-Smith J. *Internal fluid flow - the fluid dynamics of flow in pipes and ducts*. Oxford: Clarendon Press; 1980.
25. Culbertson CT, Jacobson SC, Ramsey JM. Diffusion coefficient measurements in microfluidic devices. *Talanta*. 2002;56:365–373.

Manuscript received Feb. 8, 2007, and revision received Oct. 17, 2007.